Statistical Image Reconstruction for Polyenergetic X-Ray Computed Tomography

Idris A. Elbakri* and Jeffrey A. Fessler, *Senior Member, IEEE*

***Abstract*—This paper describes a statistical image reconstruction method for X-ray computed tomography (CT) that is based on a physical model that accounts for the polyenergetic X-ray source spectrum and the measurement nonlinearities caused by energy-dependent attenuation. We assume that the object consists of a given number of nonoverlapping materials, such as soft tissue and bone. The attenuation coefficient of each voxel is the product of its unknown density and a known energy-dependent mass attenuation coefficient. We formulate a penalized-likelihood function for this polyenergetic model and develop an ordered-subsets iterative algorithm for estimating the unknown densities in each voxel. The algorithm monotonically decreases the cost function at each iteration when one subset is used. Applying this method to simulated X-ray CT measurements of objects containing both bone and soft tissue yields images with significantly reduced beam hardening artifacts.**

***Index Terms*—Beam hardening, penalized likelihood, statistical reconstruction, X-ray CT.**

I. Introduction

X-RAY computed tomography (CT) provides images of object attenuation characteristics. CT scanners record "projection" measurements of the transmission of X-ray photons through an object at different angles.

The linear attenuation coefficient $\mu(x, y, z, \mathcal{E})$ characterizes the overall attenuation property of an object. It depends on the spatial coordinates (x, y, z) and the beam energy $\mathcal{E}$, and has units of inverse distance. For a ray L_i of infinitesimal width, the projection measurement Y_i recorded by the ith detector would ideally be

$$Y_i = \int I_i(\mathcal{E}) \exp\left(-\int_{L_i} \mu(x, y, z, \mathcal{E})\, dl\right) d\mathcal{E}. \quad (1)$$

The integral in the exponent is taken over the line L_i and $I_i(\mathcal{E})$ incorporates the energy dependence of both the incident ray source spectrum and the detector sensitivity. The goal of any CT algorithm is to reconstruct the attenuation map μ from the set of measured projection data $\{Y_i\}_{i=1}^N$, where N is the number of rays. In reality, the measurements suffer from background events such as scatter and from noise. Most reconstruction methods ignore the polyenergetic nature of (1). This paper develops a statistical reconstruction method based on (1) [1].

The conventional method for reconstruction from projections is filtered back projection (FBP), which is used widely in both X-ray CT and in emission tomography modalities (PET and SPECT). FBP is based on the Fourier Slice Theorem and can be implemented with fast Fourier transform. FBP is, therefore, fast and reliable. However, the technology progress toward non-radon scanning geometries, such as cone-beam and multislice helical CT, is increasingly challenging the capabilities of FBP. Statistical methods naturally address the shortcomings of FBP, and may become viable alternatives.

Statistical techniques have several attractive features [2]–[4]. They statistically model the data noise, offering the potential for better bias-variance performance. They can also model such phenomena as scatter and energy dependence leading to more accurate and artifact-free reconstruction. Statistical methods also easily incorporate the system geometry, detector response, object constraints and any prior knowledge. They are well suited for arbitrary geometries and situations with truncated data. Their main drawback (when compared to FBP) is longer computation times. For clinical CT images with typical sizes of 512×512 pixels or larger, conventional statistical methods require prohibitively long computation times which hinder their use. In this paper, we apply ordered subsets to accelerate the algorithms [3], [5], [6].

Statistical techniques are more widely used for PET and SPECT imaging than X-ray CT. Contributing to this success is the fact that the ML expectation-maximization (ML-EM) algorithm has a closed-form expression for the emission case [7]. Also, PET and SPECT typically have low counts. The emission modalities have image sizes and resolution requirements such that the relatively longer computational time of statistical methods is fairly easily surmounted.

Statistical methods have also found their way into transmission tomography applications. One example is attenuation map reconstruction from monoenergetic, radioisotope-based transmission scans for attenuation correction of emission images [5], [8]. Statistical reconstruction for X-ray CT was shown to outperform FBP in metal artifact reduction [9], [10], in limited-angle tomography and to have lower bias-noise curves [12].

A number of X-ray CT statistical reconstruction techniques employ the EM algorithm [13]. The transmission EM algorithm does not have a closed form, forcing the use of mathematical approximations [7], [14], [15]. On occasion the emission EM algorithm has been used to reconstruct log-processed transmission data [10], [11]. This approach uses a model that mismatches the data and, therefore, leads to suboptimal results [5]. Other approaches include using coordinate descent [16] or Gauss–Seidel

Manuscript received June 20, 2001; revised January 7, 2002. This work was supported in part by the National Institutes of Health (NIH) under Grant R01CA/HL60711-06. The Associate Editor responsible for coordinating the review of this paper and recommending its publication was G. Wang. *Asterisk indicates corresponding author.*

*I. A. Elbakri is with the Electrical Engineering and Computer Science Department, 4240 EECS Building, University of Michigan, Ann Arbor, MI 48109-2122 USA (e-mail: ielbakri@umich.edu).

J. A. Fessler is with the Electrical Engineering and Computer Science Department, University of Michigan, Ann Arbor, MI 48109-2122 USA.

Publisher Item Identifier S 0278-0062(02)02936-1.

[17] algorithms to maximize a likelihood function or an approximation thereof.

Nearly all prior statistical X-ray CT reconstruction algorithms assume (either implicitly or explicitly [15]) monoenergetic X-ray beams and, thus, ignore the issue of beam hardening artifacts. That statistical methods can correct for beam hardening was anticipated early on [14], but little work appeared in this area.

Using monoenergetic photon sources would eliminate beam hardening artifacts but is impractical for diagnostic CT because of signal-to-noise ratio (SNR) considerations. Beam hardening correction methods are, therefore, necessary for reconstructing artifact-free attenuation coefficient images from polyenergetic measurements.

Many beam hardening correction methods are based on classifying the object materials into two categories: low-density (soft tissue) and high-density (bone). They also involve some estimate of the nonlinear effects and are often implemented with a parallel or fan-beam geometry in mind [18]–[20]. Recently, some of these methods were generalized to three base materials [21] and cone-beam geometry [22].

There are a variety of schemes for eliminating beam hardening artifacts in FBP images. Existing methods fall into three categories: 1) dual-energy imaging; 2) preprocessing of projection data; and 3) postprocessing of the reconstructed image.

Dual-energy imaging has been described as the most theoretically elegant approach to eliminate beam hardening artifacts [23]. The approach is based on writing the attenuation coefficient as a weighted sum of two spectral basis functions [24], one modeling the photo-electric effect and the other Compton scatter. This technique provides complete energy dependent information for CT imaging. An attenuation coefficient image can in principle be presented at any energy, free from beam hardening artifacts. The method's major drawback is the requirement for two independent energy measurements. This has inhibited its use in clinical applications, despite the potential diagnostic benefit of energy information. Recently, multienergy X-ray CT has been used for imaging small animals [25] with a CT scanner that was custom built with an energy-selective detector. Dual-energy imaging is also an area where statistical iterative reconstruction provides superior results to analytical methods [26].

Preprocessing approaches are based on the assumption that the energy dependence of soft tissue is similar to that of water. Knowledge of the energy dependence of the attenuation coefficient of water provides a one-to-one mapping between monoenergetic and polyenergetic measurements. In preprocessing, one simply maps (or precorrects) the sinogram data to monoenergetic values and then one reconstructs the image from the corrected sinogram. Preprocessing works well with soft-tissue objects, but is poor when high Z materials, such as bone, are present. Preprocessing is often the first step in bone correction algorithms [18], [20].

The method described by Joseph and Spital (henceforth, referred to as JS) [18] is a postprocessing technique that corrects for soft tissue and high Z material (bone) distortions. The method requires knowledge of the X-ray spectrum and involves an initial reconstruction, segmentation, linearization and a final reconstruction. It has been generalized to correct for three-substance beam hardening, the third substance usually being a contrast agent such as Iodine [21]. A variation of that algorithm [22] corrects for beam-hardening artifacts in cone-beam geometry. It uses a tilted parallel geometry to correct the artifacts. The tilted parallel geometry reduces the computational complexity involved in the forward projection and back-projection reconstruction steps for the cone-beam geometry.

Yan *et al.* developed an iterative, but nonstatistical, beam hardening correction method [27]. It assumes the attenuation coefficient at each pixel is a linear combination of the attenuation coefficients of two base substances. The algorithm iteratively computes the fraction of each base substance at each pixel. The algorithm requires *a priori* knowledge of the two base substances at each pixel, in addition to the X-ray spectrum.

The approach we propose for beam hardening correction is a statistical iterative reconstruction algorithm [1]. It requires knowledge of the X-ray spectrum and requires a presegmented initial image (usually obtainable from a good FBP image) like JS. The algorithm iteratively minimizes surrogate functions to the Poisson likelihood and can use ordered subsets to accelerate convergence. Depending on the approximations used, one version of the algorithm is monotonic. The algorithm can also take scatter estimates into account.

Recently, De Man *et al.* suggested an alternative statistical iterative approach [28]. This technique models the object as a linear combination of the spectral properties of two base substances, usually water and bone. Knowledge of the X-ray spectrum is necessary, but a presegmented image is not required. There are differences in the object models used in De Man's approach and ours that would be interesting to compare in the future. Our derivation uses paraboloidal surrogates in a way that can guarantee algorithm monotonicity even with nonzero scatter background [r_i in (39) below]. The algorithm in [28] does not use surrogate functions. It minimizes the Poisson likelihood directly but is derived without taking scatter into account. The ordered-subset versions of both approaches are not monotonic and probably roughly equivalent other than the differences in the object model.

This paper is organized as follows. Section II discusses a physical model and summarizes a "conventional" statistical algorithm based on a monoenergetic X-ray beam assumption. Section III generalizes the model and derives algorithms based on the more realistic polyenergetic case. In Section IV, we present simulation results that compare uncorrected FBP, JS-corrected FBP, statistical monoenergetic reconstruction, and statistical polyenergetic reconstruction. Section V discusses the results and outlines potential future work.

II. Monoenergetic Transmission Reconstruction

In this section, we describe the physical and statistical models for the problem of transmission image reconstruction with monoenergetic beams. The statistical reconstruction method involves maximizing a penalized-likelihood (PL) objective function. Presenting the monoenergetic case illustrates our notation and some key ideas of statistical iterative reconstruction before having to deal with the complexities of polyenergetic physics.

A. Monoenergetic Model

Under the assumption of a monoenergetic beam, i.e., $I_i(\mathcal{E}) = I_i(\mathcal{E}_o)\delta(\mathcal{E}-\mathcal{E}_o)$, the measurement (under ideal conditions) simplifies to Beer's law

$$Y_i = I_i(\mathcal{E}_o)\exp\left(-\int_{L_i}\mu(x, y, z, \mathcal{E}_o)dl\right). \quad (2)$$

We parameterize the image in object space (attenuation coefficient) using square pixels. The goal of the algorithm becomes to estimate the value of the (discretized) attenuation coefficient at those pixels. Let $\mu = [\mu_1, \ldots, \mu_p]'$ be the vector of unknown attenuation coefficients having units of inverse length, where $'$ denotes transpose. We model the measurements as independently distributed Poisson random variables [4] that are contaminated by extra background counts, caused primarily by scatter. Additive detector read-out noise can be accounted for in a several ways [29]. We assume the following statistical model for the measurements:

$$Y_i \sim \text{ Poisson } \left\{b_i e^{-[\mathbf{A}\mu]_i} + r_i\right\}, \qquad i = 1, \ldots, N \quad (3)$$

where $b_i = I_i(\mathcal{E}_o)$ is the blank scan factor and N is the number of measured rays. The notation $[\mathbf{A}\mu]_i = \sum_{j=1}^{p} a_{ij}\mu_j$ represents the ith line integral. The $N \times p$ matrix $\mathbf{A} = \{a_{ij}\}$ is the system matrix which accounts for the system geometry as well as any other significant physical effects such as detector response. For ray i and pixel j, a_{ij} is the area of overlap between the ray beam and the pixel, normalized by the detector width, and has units of length. The term r_i accounts for the mean number of background events and read-out noise variance [29]. We assume that $\{b_i\}$, $\{r_i\}$, and $\{a_{ij}\}$ are known nonnegative constants [4].

To estimate the attenuation coefficient vector μ, we use a likelihood-based estimation approach. The Poisson log-likelihood for independent measurements is given by

$$L(\mu) = \sum_{i=1}^{N}\left\{Y_i \log\left(b_i e^{-[\mathbf{A}\mu]_i} + r_i\right) - \left(b_i e^{-[\mathbf{A}\mu]_i} + r_i\right)\right\} \quad (4)$$

ignoring constant terms. When $\mathbf{A}$ has full column rank and the data is noise-free, maximizing the likelihood would give a perfect result. In reality, the data is noisy and maximum likelihood (ML) will give a very noisy reconstruction due to the ill-posedness of the problem, hence, the need for regularization.

We regularize by adding to the likelihood a penalty term that penalizes difference in the values of neighboring pixels. The regularizing penalty term is given by the following:

$$R(\mu) = \sum_{j=1}^{p}\sum_{k\in\mathcal{N}_j}\psi(\mu_j - \mu_k) \quad (5)$$

where ψ is a potential functions and $\mathcal{N}_j$ is some neighborhood of pixel j. We use the convex edge-preserving Huber penalty

$$\psi(x;\delta) = \begin{cases} \dfrac{x^2}{2}, & x < \delta \\ \delta|x| - \dfrac{\delta^2}{2}, & x \geq \delta. \end{cases} \quad (6)$$

Combining the likelihood with a penalty gives a PL objective function

$$\Phi(\mu) = L(\mu) - \beta R(\mu) \quad (7)$$

where β is a scalar that controls the tradeoff between the data-fit and the penalty terms. The goal of the reconstruction technique becomes to maximize (7) subject to certain object constraints such as nonnegativity

$$\hat{\mu} = \arg\max_{\mu\geq 0}\Phi(\mu). \quad (8)$$

Section II-B will discuss an iterative technique for approximately solving (8).

B. Penalized Weighted Least Squares With Ordered Subsets

The algorithm is formulated using a quadratic approximation to the Poisson likelihood, which leads to a simpler objective function [17]. The quadratic approximation leads to a penalized weighted-least-squares (PWLS) estimate. For high data SNR, PWLS leads to negligible bias [30] and the simpler objective function can reduce computation time.

For convenience, we write the negative log-likelihood corresponding to (4) as follows:

$$-L(\mu) = \sum_{i=1}^{N} g_i([\mathbf{A}\mu]_i) \quad (9)$$

where

$$g_i(l) = -Y_i \log(b_i e^{-l} + r_i) + (b_i e^{-l} + r_i). \quad (10)$$

Applying a second-order Taylor's expansion to $g_i(l)$ around an estimate $\hat{l}_i$ of the line integral yields [17]

$$g_i(l) \approx g_i\left(\hat{l}_i\right) + \dot{g}_i\left(\hat{l}_i\right)\left(l - \hat{l}_i\right) + \frac{\ddot{g}_i\left(\hat{l}_i\right)}{2}\left(l - \hat{l}_i\right)^2 \quad (11)$$

where $\dot{g}_i$ and $\ddot{g}_i$ are the first and second derivatives of g_i. Assuming $Y_i > r_i$, we can estimate the line integral with

$$\hat{l}_i = \log\left(\frac{b_i}{Y_i - r_i}\right). \quad (12)$$

Substituting this estimate into (11) gives the following approximation for g_i:

$$g_i(l) \approx (Y_i - Y_i \log Y_i) + \frac{w_i}{2}\left(l - \hat{l}_i\right)^2. \quad (13)$$

The first term in (13) is independent of l and can be dropped. The weight is $w_i = (Y_i - r_i)^2/Y_i$ or zero for any i where $Y_i \leq r_i$. The resulting PWLS cost function is

$$\Phi(\mu) = \sum_{i=1}^{N}\frac{w_i}{2}\left([\mathbf{A}\mu]_i - \hat{l}_i\right)^2 + \beta R(\mu). \quad (14)$$

The penalty term may be nonquadratic.

According to the optimization transfer principle [4], [31], [32], rather than minimizing the cost function (14), one can replace $\Phi(\mu)$ with a surrogate function $\phi(\mu; \mu^n)$ that is easier to minimize. For monotonicity, the surrogate must be chosen such that $\phi(\mu^n; \mu^n) = \Phi(\mu^n)$ and $\phi(\mu; \mu^n) \geq \Phi(\mu)$ [4]. A new surrogate function is used at each iteration.

The surrogate we seek is one that will make the cost function separable, so that all pixels can be updated simultaneously. Toward that end, we exploit the convexity of the data-fit term in (14). Rewrite the line integral as follows [31], [32]:

$$[\mathbf{A}\mu]_i = \sum_{j=1}^{p} a_{ij}\mu_j = \sum_{j=1}^{p} \alpha_{ij} \left\{ \frac{a_{ij}}{\alpha_{ij}} (\mu_j - \mu_j^n) + [\mathbf{A}\mu^n]_i \right\} \quad (15)$$

where

$$\sum_{j=1}^{p} \alpha_{ij} = 1, \qquad \forall i,\ \alpha_{ij} \geq 0. \quad (16)$$

By convexity

$$\left([\mathbf{A}\mu]_i - \hat{l}_i \right)^2 \leq \sum_{j=1}^{p} \alpha_{ij} \left(\frac{a_{ij}}{\alpha_{ij}} (\mu_j - \mu_j^n) + [\mathbf{A}\mu^n]_i - \hat{l}_i \right)^2.$$

Applying this to (14) yields the following separable surrogate:

$$Q(\mu;\, \mu^n) = \sum_{i=1}^{N} \sum_{j=1}^{p} \alpha_{ij} \frac{w_i}{2} \times \left(\frac{a_{ij}}{\alpha_{ij}} (\mu_j - \mu_j^n) + [\mathbf{A}\mu^n]_i - \hat{l}_i \right)^2. \quad (17)$$

A similar development can be pursued for the convex penalty term $R(\mu)$ yielding a separable penalty surrogate [32], denoted $S(\mu;\, \mu^n)$. We now seek to minimize the new separable global surrogate

$$\phi(\mu;\, \mu^n) \triangleq Q(\mu;\, \mu^n) + \beta S(\mu;\, \mu^n). \quad (18)$$

Since the surrogate is a separable paraboloid, it can be easily minimized by zeroing the first derivative. This leads to the following simultaneous update algorithm:

$$\mu_j^{n+1} = \left[\mu_j^n - \frac{\left. \frac{\partial \phi(\mu;\mu^n)}{\partial \mu_j} \right|_{\mu=\mu^n}}{\left. \frac{\partial^2 \phi(\mu;\mu^n)}{\partial \mu_j^2} \right|_{\mu=\mu^n}} \right]_+, \qquad j = 1, \ldots, p \quad (19)$$

where $[\cdot]_+$ enforces nonnegativity. The first and second derivatives of the surrogate are easily shown to be

$$\left. \frac{\partial \phi(\mu;\, \mu^n)}{\partial \mu_j} \right|_{\mu=\mu^n} = \sum_{i=1}^{N} a_{ij} w_i \left([\mathbf{A}\mu^n]_i - \hat{l}_i \right) + \beta \left. \frac{\partial S}{\partial \mu_j} \right|_{\mu=\mu^n} \quad (20)$$

$$\left. \frac{\partial^2 \phi(\mu;\, \mu^n)}{\partial \mu_j^2} \right|_{\mu=\mu^n} = \sum_{i=1}^{N} \frac{a_{ij}^2 w_i}{\alpha_{ij}} + \beta \left. \frac{\partial^2 S}{\partial \mu_j^2} \right|_{\mu=\mu^n}. \quad (21)$$

To make the denominator in (19) small (and, hence, the step size large), we want $\{\alpha_{ij}\}$ to be large, subject to (16). We also want $\{\alpha_{ij}\}$ to be independent of the current iterate (so that it can be precomputed) [2]. One convenient choice is

$$\alpha_{ij} = \frac{a_{ij}}{\sum_{j=1}^{p} a_{ij}}. \quad (22)$$

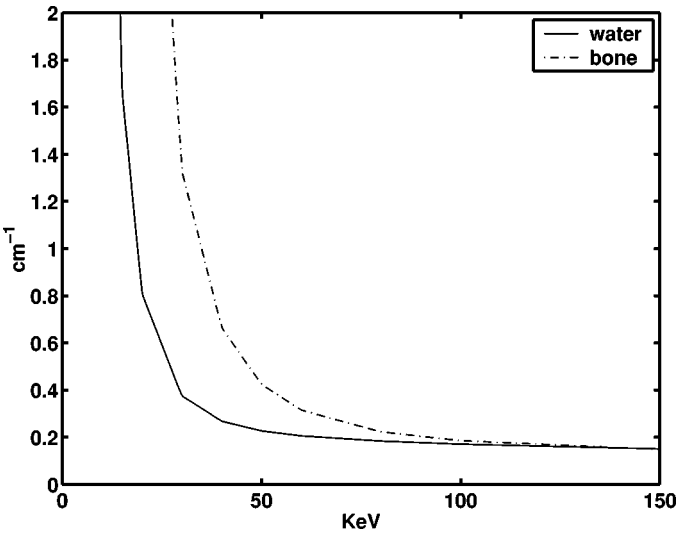

Fig. 1. Linear attenuation coefficient energy dependence of water and bone.

Both the numerator and denominator in (19) involve backprojecting over sinogram bins. In the spirit of similar work [3], [5], [6], we use ordered subsets to accelerate algorithm "convergence" by a factor proportional to the number of subsets [6]. We call this method the penalized weighted least squares ordered subsets (PWLS-OS) algorithm for transmission tomography. With M subsets, the PWLS-OS update equation is

$$\hat{\mu}_j = \left[\hat{\mu}_j - \frac{M \sum_{i \in S} a_{ij} w_i \left([\mathbf{A}\hat{\mu}]_i - \hat{l}_i \right) + \beta \left. \frac{\partial S}{\partial \mu_j} \right|_{\mu=\mu_{old}}}{\sum_i \frac{a_{ij}^2 w_i}{\alpha_{ij}} + \beta \left. \frac{\partial^2 S}{\partial \mu_j^2} \right|_{\mu=\mu_{old}}} \right]_+.$$

We have found that this algorithm works quite well for moderate to high SNR monoenergetic measurements. However, as shown in Figs. 3 and 6 below, when applied to polyenergetic data, it yields artifacts similar to those of FBP, which is also based on a monoenergetic model.

The next section presents a polyenergetic model and substantially generalizes the iterative algorithm accordingly. The useful concepts of optimization transfer, separability etc. also readily apply to the polyenergetic case.

III. Polyenergetic X-Ray CT

Algorithms such as the one derived in the previous section ignore the polyenergetic nature of the X-ray beam and the energy dependence of the attenuation coefficient. With a polyenergetic source, the measurement Y_i along path L_i is given by (1). Nonlinear beam hardening artifacts result if one ignores the energy dependence of the measurements [18], [23], [33]. Fig. 1 shows the energy dependence of the attenuation coefficients of water (density 1.0 gm/cm^3) and bone (density 1.92 gm/cm^3). A hard X-ray beam is one with higher average energy [35]. Beam hardening is a process whereby the average energy of the X-ray beam increases as the beam propagates through a material since lower energy X-rays are preferentially attenuated. X-rays traversing different paths through an object will emerge with different spectra, leading to inconsistencies in the data (in the Radon sense), hence, the artifacts shown in Fig. 3.

Beam hardening generally leads to a reduction in the reconstructed attenuation coefficient [33]. Thick bones also generate dark streaks [24]. In soft tissue, the values are depressed nonuniformly, leading to what has been termed "cupping." In addition, bone areas can "spill over" into soft tissue, leading to a perceived increase in the attenuation coefficient [18].

In this section, we summarize a model for polyenergetic X-ray CT and then develop an iterative reconstruction algorithm based on it that overcomes the artifacts produced by conventional methods.

A. Polyenergetic Statistical Model for X-Ray CT

We assume that the object is comprised of K known nonoverlapping material types. We also assume that the material class of each voxel is known. These classes can be determined by segmenting a FBP reconstruction that has been "corrected" for beam hardening effects [18]. The method of Joseph and Spital requires a similar kind of segmentation, usually obtained from a soft-tissue-corrected image [18]. For the kth material type, we model the attenuation coefficient of the jth voxel as the product of the (known) energy-dependent *mass* attenuation coefficient $m_k(\mathcal{E})$ (cm^2/g) and the (unknown) energy-independent density ρ_j (g/cm^3) [18], [24], [26]. Expressed mathematically in the discrete domain

$$\mu_j(\mathcal{E}) = \sum_{k=1}^{K} m_k(\mathcal{E}) \rho_j f_j^k \tag{23}$$

where $f_j^k = 1$ if the jth voxel belongs to the kth material type and $f_j^k = 0$ otherwise.

We again denote the system matrix by $\mathbf{A} = \{a_{ij}\}$ and make the following definitions:

$$a_{ij}^k \triangleq a_{ij} f_j^k \tag{24}$$

$$\mathbf{A^k} = \{a_{ij}^k\} \tag{25}$$

$$s_i^k(\rho) \triangleq \int_{L_i} \rho(x, y) f^k(x, y)\, dl = \sum_{j=1}^{p} a_{ij}^k \rho_j \tag{26}$$

$$\underline{s}_i(\rho) = [s_i^1(\rho), s_i^2(\rho), \ldots, s_i^K(\rho)]'. \tag{27}$$

We assume that the mass attenuation coefficients $\{m_k(\mathcal{E})\}_{k=1}^K$ of the K materials are known. From (1), (23), and the definitions above, the mean of the measured data along path L_i is

$$\begin{aligned} E[Y_i] &= \int I_i(\mathcal{E}) \exp\left(-\sum_{k=1}^{K} m_k(\mathcal{E}) s_i^k(\rho) \right) d\mathcal{E} + r_i \\ &= \overline{Y}_i(\underline{s}_i(\rho)) + r_i \end{aligned} \tag{28}$$

where

$$\overline{Y}_i(\underline{s}) \triangleq \int I_i(\mathcal{E}) e^{-\underline{m}'(\mathcal{E})\underline{s}}\, d\mathcal{E}$$

and $\underline{m}'(\mathcal{E}) = [m_1(\mathcal{E}), \ldots, m_K(\mathcal{E})]$. We have expressed the measurements in terms of the vector function $\underline{s}_i$ which has as its elements the line integrals of the K different material densities. Given the X-ray spectrum, we tabulate the values of $\overline{Y}_i(\cdot)$ and its gradient $\nabla \overline{Y}_i(\cdot) = [(\partial \overline{Y}_i/\partial s^1), \ldots, (\partial \overline{Y}_i/\partial s^K)]$ over the range of arguments $[s^1, \ldots, s^K]$ that correspond to representative objects.

The goal of the algorithm is to estimate the density coefficient vector $\rho = [\rho_1, \ldots, \rho_p]'$. Rather than estimating K vector quantities of length p, each representing the density of one material, the assumption of nonoverlapping materials enables us to keep the number of unknowns equal to p, as is the case in the monoenergetic model. This is possible only if prior segmentation of the object is available. This segmentation is also necessary for the JS technique [18].

B. Polyenergetic Model Cost Function

We now express the Poisson negative log-likelihood in terms of the vector density ρ and the vector function $\underline{s}_i$. To derive the algorithm, we use the optimization transfer principle three times: first using the multiplicative convexity property [31]; second using parabola surrogates [4] and lastly De Pierro's additive convexity trick [32]. The successive applications of the optimization transfer principle yield a separable and simple surrogate function that is easier to minimize than the negative log-likelihood.

Recall that the function $\overline{Y}_i(\underline{s}_i(\rho))$ in (28) represents the ideal expected value of the measurement Y_i at the ith detector. Using $\overline{Y}_i$ in (4) gives the following negative log-likelihood in the polyenergetic case:

$$-L(\rho) = \sum_{i=1}^{N} h_i\left(\overline{Y}_i(\underline{s}_i(\rho)) + r_i\right) \tag{29}$$

$$h_i(t) \triangleq -Y_i \log t + t. \tag{30}$$

The reconstruction problem now is to find an estimate $\hat{\rho}$ such that

$$\hat{\rho} = \arg\min_{\rho \geq 0} \Phi(\rho) \tag{31}$$

where

$$\Phi(\rho) = -L(\rho) + \beta R(\rho). \tag{32}$$

The regularization term can be treated exactly as in Section II-B or it can be modified to avoid smoothing between different tissue types. For simplicity in this presentation, we focus on the likelihood term. An iterative algorithm is needed to perform the minimization (31).

The difficulty arises with the argument of $h_i(\cdot)$, which is nonlinear in (29). Our first goal is to move the integral in (28) outside the (convex) function h_i. Toward that end, define

$$t_i(\mathcal{E}, \underline{s}) \triangleq e^{-\underline{m}'(\mathcal{E})\underline{s}} + \overline{r}_i \tag{33}$$

$$\overline{r}_i \triangleq \frac{r_i}{\int I_i(\mathcal{E})\, d\mathcal{E}} \tag{34}$$

$$b_i^n(\mathcal{E}) \triangleq \frac{\overline{Y}_i(\underline{s}_i^n)}{t_i(\mathcal{E}, \underline{s}_i^n)} \tag{35}$$

where $\underline{s}_i^n = \underline{s}_i(\rho^n)$. With the above definitions and (28)

$$\begin{aligned} \overline{Y}_i(\underline{s}) + r_i &= \int I_i(\mathcal{E}) t_i(\mathcal{E}, \underline{s})\, d\mathcal{E} \\ &= \int \frac{I_i(\mathcal{E})}{b_i^n(\mathcal{E})} t_i(E, \underline{s}) b_i^n(\mathcal{E})\, d\mathcal{E}. \end{aligned} \tag{36}$$

Since

$$\int \frac{I_i(\mathcal{E})}{b_i^n(\mathcal{E})}\, d\mathcal{E} = 1 \tag{37}$$

$$\frac{I_i(\mathcal{E})}{b_i^n(\mathcal{E})} \geq 0 \tag{38}$$

we can use the convexity of the function $h_i(t)$ in (30) as follows [31], [36]:

$$\begin{aligned} h_i(\overline{Y}_i(\underline{s}) + r_i) &= h_i\left(\int \frac{I_i(\mathcal{E})}{b_i^n(\mathcal{E})}\, t_i(\mathcal{E}, \underline{s}) b_i^n(\mathcal{E})\, d\mathcal{E}\right) \\ &\leq \int \frac{I_i(\mathcal{E})}{b_i^n(\mathcal{E})}\, h_i\left(t_i(\mathcal{E}, \underline{s}) b_i^n(\mathcal{E})\right)\, d\mathcal{E}. \end{aligned}$$

Combining with (29) gives the following surrogate Q_1 for the negative of the polyenergetic log-likelihood

$$-L(\rho) = \sum_{i=1}^{N} h_i(\overline{Y}_i(\underline{s}_i(\rho)) + r_i) \tag{39}$$

$$\leq \sum_{i=1}^{N} \int \frac{I_i(\mathcal{E})}{b_i^n(\mathcal{E})}\, h_i\left(t_i(\mathcal{E}, \underline{s}_i(\rho)) b_i^n(\mathcal{E})\right)\, d\mathcal{E}$$

$$\triangleq Q_1(\rho; \rho^n). \tag{40}$$

It is straightforward to verify that Q_1 satisfies the conditions of the optimization transfer principle [37]. The surrogate Q_1 is simpler than the actual likelihood because the energy integral is outside of the log operation. It is not, however, quadratic. We next apply optimization transfer to Q_1 to derive a paraboloidal surrogate. Such a surrogate is desirable because it is easily minimized. The first step is to express h_i using a quadratic surrogate

$$\begin{aligned} h_i(t_i(\mathcal{E}, \underline{s}) b_i^n(\mathcal{E})) &= h_i\left(b_i^n(\mathcal{E}) e^{-\underline{m}'(\mathcal{E})\underline{s}} + b_i^n(\mathcal{E})\overline{r}_i\right) \\ &\triangleq g_i^n(\underline{m}'(\mathcal{E})\underline{s}, \mathcal{E}) \\ &\leq q_i^n(\underline{m}'(\mathcal{E})\underline{s}, \mathcal{E}) \end{aligned} \tag{41}$$

where

$$\begin{aligned} q_i^n(l, \mathcal{E}) = g_i^n(l_i^n, \mathcal{E}) + \dot{g}_i^n(l_i^n, \mathcal{E})(l - l_i^n) \\ + \tfrac{1}{2} C_i^n(\mathcal{E})(l - l_i^n)^2. \end{aligned} \tag{42}$$

We must choose the curvature $C_i^n(\mathcal{E})$ to ensure that $q_i^n(l, \mathcal{E})$ satisfies the conditions for a surrogate (if we seek a monotone algorithm). Combining (41) and (40), the overall paraboloidal surrogate is

$$Q_2(\rho; \rho^n) = \sum_{i=1}^{N} \int \frac{I_i(\mathcal{E})}{b_i^n(\mathcal{E})}\, q_i^n(\underline{m}'(\mathcal{E})\underline{s}_i(\rho), \mathcal{E})\, d\mathcal{E}. \tag{43}$$

Next, we derive a separable surrogate which, similar to the monoenergetic case, lends itself easily to parallelization. We apply De Pierro's additive convexity trick that we used in (15) with the monoenergetic case [31], [32]. First, define

$$\lambda_{ij}(\mathcal{E}) \triangleq \sum_{k=1}^{K} m_k(\mathcal{E}) a_{ij}^k$$

$$\mathbf{\Lambda}(\mathcal{E}) \triangleq \{\lambda_{ij}(\mathcal{E})\}.$$

We rewrite the density line integrals as follows:

$$\begin{aligned} \underline{m}'(\mathcal{E})\,\underline{s}_i(\rho) &= \sum_{j=1}^{p} \sum_{k=1}^{K} m_k(\mathcal{E}) a_{ij}^k \rho_j = \sum_{j=1}^{p} \lambda_{ij}(\mathcal{E})\rho_j \\ &= \sum_{j=1}^{p} \alpha_{ij} \left(\frac{\lambda_{ij}(\mathcal{E})}{\alpha_{ij}}(\rho_j - \rho_j^n) + [\mathbf{\Lambda}(\mathcal{E})\rho^n]_i\right) \end{aligned}$$

where the α_{ij}s satisfy (16). Using the convexity of q_i^n (in its first argument) yields

$$\begin{aligned} &q_i^n(\underline{m}'(\mathcal{E})\,\underline{s}_i(\rho), \mathcal{E}) \\ &= q_i^n\left(\sum_{j=1}^{p} \alpha_{ij}\left(\frac{\lambda_{ij}(\mathcal{E})}{\alpha_{ij}}(\rho_j - \rho_j^n) + [\mathbf{\Lambda}(\mathcal{E})\rho^n]_i\right), \mathcal{E}\right) \\ &\leq \sum_{j=1}^{p} \alpha_{ij}\, q_i^n\left(\frac{\lambda_{ij}(\mathcal{E})}{\alpha_{ij}}(\rho_j - \rho_j^n) + [\mathbf{\Lambda}(\mathcal{E})\rho^n]_i, \mathcal{E}\right). \end{aligned} \tag{44}$$

The final separable paraboloidal surrogate to minimize is

$$\begin{aligned} Q(\rho; \rho^n) = \sum_{j=1}^{p} \sum_{i=1}^{N} \int \frac{I_i(\mathcal{E})}{b_i^n(\mathcal{E})}\, \alpha_{ij} q_i^n \\ \left(\frac{\lambda_{ij}(\mathcal{E})}{\alpha_{ij}}(\rho_j - \rho_j^n) + [\mathbf{\Lambda}(\mathcal{E})\rho^n]_i, \mathcal{E}\right) d\mathcal{E}. \end{aligned} \tag{45}$$

C. Iterative Algorithm for Polyenergetic CT

To derive the actual algorithm, take the first derivative of the surrogate and set it equal to zero. This gives an update expression similar to that in (19) (ignoring regularization)

$$\rho_j^{n+1} = \left[\rho_j^n - \frac{\left.\frac{\partial Q(\rho; \rho^n)}{\partial \rho_j}\right|_{\rho=\rho^n}}{\left.\frac{\partial^2 Q(\rho; \rho^n)}{\partial \rho_j^2}\right|_{\rho=\rho^n}}\right]_+, \qquad j = 1, \ldots, p. \tag{46}$$

The derivatives of the surrogate, evaluated at the current iterate ρ^n are

$$\begin{aligned} \left.\frac{\partial Q}{\partial \rho_j}\right|_{\rho=\rho^n} &= \sum_{i=1}^{N} \int \frac{I_i(\mathcal{E})}{b_i^n(\mathcal{E})}\, \lambda_{ij}(\mathcal{E}) \dot{g}_i^n(\underline{m}'(\mathcal{E})\underline{s}_i^n, \mathcal{E})\, d\mathcal{E} \\ &= \sum_{i=1}^{N} \left(\frac{Y_i}{\overline{Y}_i(\underline{s}_i^n)} - 1\right) \\ &\quad \times \int \lambda_{ij}(\mathcal{E}) I_i(\mathcal{E}) e^{-\underline{m}'(\mathcal{E})\underline{s}_i^n}\, d\mathcal{E} \\ &= \sum_{i=1}^{N} \sum_{k=1}^{K} a_{ij} f_j^k \left(\frac{Y_i}{\overline{Y}_i(\underline{s}_i^n)} - 1\right) \nabla_k \overline{Y}_i(\underline{s}_i^n) \\ &= -\left.\frac{\partial L}{\partial \rho_j}\right|_{\rho=\rho^n} \end{aligned}$$

$$\frac{\partial^2 Q}{\partial \rho_j^2} = \sum_{i=1}^{N} \int \frac{I_i(\mathcal{E})}{b_i^n(\mathcal{E})} \frac{C_i^n(\mathcal{E})}{\alpha_{ij}} \lambda_{ij}^2(\mathcal{E})\, d\mathcal{E}. \tag{47}$$

The second derivative in (47) has two terms that are iteration dependent, $b_i^n(\mathcal{E})$ and the curvature $C_i^n(\mathcal{E})$. The curvature, in particular, influences the rate of convergence of the algorithm [4]. We next explore some possibilities for it.

D. Curvature

If one desires a monotonic algorithm, then it is necessary to choose curvatures such that (42) satisfies the condition of the optimization transfer principle. A simple choice for the curvature is the maximum second derivative in the feasible region for the projections. The closed form expression for the maximum curvature is [4]

$$C_i^n(\mathcal{E}) = \left[b_i^n(\mathcal{E}) - \frac{Y_i \overline{r}_i}{(1+\overline{r}_i)^2} \right]_+ \leq [b_i^n(\mathcal{E})]_+ . \qquad (48)$$

This inequality always holds since $r_i \geq 0$ and $Y_i \geq 0$. We can use the simpler right hand side of (48) and still have a monotonic algorithm. This is equivalent to using the maximum curvature when the background term $\overline{r}_i$ is small.

The curvature affects the step size that the algorithm takes toward the minimizer. The maximum curvature results in small steps and, hence, a slowly converging algorithm. Plugging the right hand side of (48) in (47) gives the following:

$$\frac{\partial^2 Q}{\partial \rho_j^2} = \sum_{i=1}^{N} \int \frac{I_i(\mathcal{E})}{\alpha_{ij}} \lambda_{ij}^2(\mathcal{E})\, d\mathcal{E}. \qquad (49)$$

The above equation has no iteration-dependent terms and can be easily precomputed.

Another possible curvature, given in [4], is optimal in the sense that it satisfies the conditions of optimization transfer while keeping the step size as large as possible. The optimal curvature must be computed at every iteration. It, therefore, accelerates convergence, but requires more computation per iteration.

E. Precomputed Curvature

By relaxing the monotonicity requirement, we can develop faster algorithms. Since we use ordered subsets to implement the algorithms, monotonicity is compromised anyway.

We can choose a curvature in (42) such that $q_i^n(l, \mathcal{E}) \approx g_i^n(l, \mathcal{E})$, rather than requiring inequality. In this case, the paraboloids are quadratic approximations to the likelihood that are updated at every iteration [unlike (11)]. A reasonable curvature to use is the second derivative of g_i^n evaluated at the point that minimizes the function, $l_i^{\min} = \log(b_i^n(\mathcal{E})/(Y_i - b_i^n(\mathcal{E})\overline{r}_i))$. The curvature becomes

$$C_i^n(\mathcal{E}) = \ddot{g}_i^n \left(\log \frac{b_i^n(\mathcal{E})}{Y_i - b_i^n(\mathcal{E})\overline{r}_i}, \mathcal{E} \right) \approx Y_i. \qquad (50)$$

To simplify matters further, define

$$\mathcal{E}_{\text{eff}} \triangleq \frac{\int \mathcal{E} I_i(\mathcal{E})\, d\mathcal{E}}{\int I_i(\mathcal{E})\, d\mathcal{E}} \qquad (51)$$

as the effective energy of the X-ray beam. We now make the approximation of evaluating $\lambda_{ij}(\mathcal{E})$ in (47) at $\mathcal{E}_{\text{eff}}$ and pull it out of the integral. The remaining energy terms integrate to unity. With the assumption of nonoverlapping materials and

$$\alpha_{ij} = \frac{\sum_k a_{ij}^k}{\sum_k \sum_j a_{ij}^k} = \frac{a_{ij}}{\sum_j a_{ij}} = \frac{a_{ij}}{\gamma_i}$$

the second derivative reduces to

$$\frac{\partial^2 Q}{\partial \rho_j^2} \approx \sum_{i=1}^{N} \frac{\lambda_{ij}^2(\mathcal{E}_{\text{eff}})}{\alpha_{ij}} Y_i \approx \sum_{k=1}^{K} m_k^2(\mathcal{E}_{\text{eff}}) \sum_{i=1}^{N} a_{ij}\gamma_i Y_i \triangleq d_j. \qquad (52)$$

This expression is completely independent of iteration. It can be precomputed and stored, further accelerating the algorithm. The following is the overall ordered subsets version of the algorithm.

- Precompute d_j using (52).
- Tabulate $\overline{Y}_i(\cdot)$ and $\nabla\overline{Y}_i(\cdot)$ over an appropriate range of break points.
- initialize with $\hat{\rho}$.
- **for** each iteration $n = 1, \ldots,$ niter
  - — **for** each subset $S = 1, \ldots, M$
    - ∗ compute $\hat{s}_i^k = \sum_{j=1}^{p} a_{ij}^k \hat{\rho}_j$ for $k = 1, \ldots, K$. Set $\underline{\hat{s}}_i = [\hat{s}_i^1, \ldots, \hat{s}_i^K]$.
    - ∗ compute $\overline{Y}_i(\underline{\hat{s}}_i)$ and $\nabla\overline{Y}_i(\underline{\hat{s}}_i)$ by interpolation from the precomputed tables.
    - ∗ evaluate

$$\hat{N}_j = \sum_{i \in S} \sum_{k=1}^{K} a_{ij} f_j^k \left(\frac{Y_i}{\overline{Y}_i(\underline{\hat{s}}_i)} - 1 \right) \nabla_k \overline{Y}_i(\underline{\hat{s}}_i)$$

    - ∗ compute for $j = 1, \ldots, p$

$$\hat{\rho}_j = \left[\hat{\rho}_j - \frac{M\hat{N}_j + \beta \left. \frac{\partial S}{\partial \rho_j} \right|_{\rho=\hat{\rho}}}{d_j + \beta \left. \frac{\partial^2 S}{\partial \rho_j^2} \right|_{\rho=\hat{\rho}}} \right]_+ \qquad (53)$$

  - — **end**
- **end**

Recall that S in (53) is the surrogate for the regularization penalty, first introduced in (18). If the optimal curvature [4] or maximum curvature (48) are used, this algorithm will monotonically decrease the cost function each iteration when one subset is used. Using ordered subsets and the precomputed curvature destroys monotonicity, but significantly accelerates progress in the early iterations.

IV. Simulation Results

We assess the effectiveness of our algorithm with simulated polyenergetic Poisson X-ray projections. We assume a parallel beam geometry, but the algorithm applies equally well to other geometries. The image field of view is 40 cm and the rotation range is 180°. The simulated measurements are free of scatter and detector readout noise.

We simulate polyenergetic transmission data with the polyenergetic spectrum (mean: 67.12 keV; standard deviation: 17.76 keV) shown in Fig. 2 and a blank scan of 4.87×10^6 counts/detector. The blank scan value is realistic and mimics a 120-kVp, 170-mAs scan protocol [38]. The spectrum was obtained from Monte Carlo simulations of the setup in [39].

We reconstruct the simulated data with FBP, monoenergetic statistical algorithm (PWLS-OS) and polyenergetic statistical algorithm. We use the soft-tissue and JS methods to remove beam hardening artifacts in the FBP image. We also pick the FBP reconstruction parameters to give comparable resolution

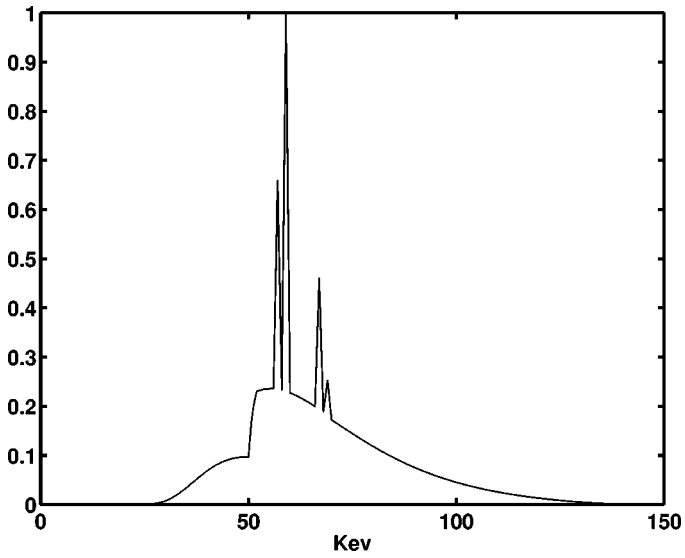

Fig. 2. Energy spectrum.

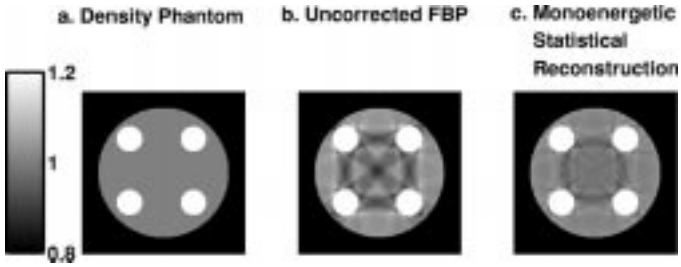

Fig. 3. Bone/water density phantom results.

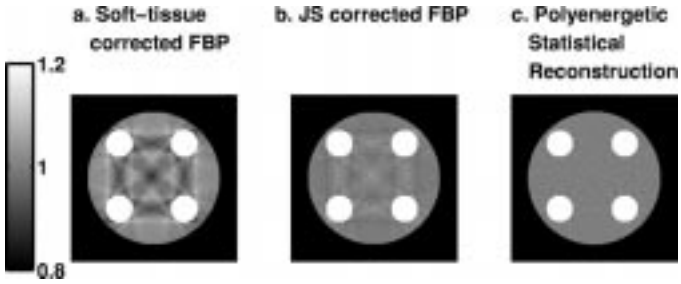

Fig. 4. Bone/water density phantom results.

and noise properties to the statistical algorithms (the statistical algorithms can perform better in this regard, but our purpose is to illustrate beam hardening correction). All runs of the statistical algorithms use a Huber penalty with $\beta = 1000$, $\delta = 0.01$ cm^{-1} for monoenergetic reconstruction, and $\delta = 0.1$ gm/cm^3 for polyenergetic reconstruction. The parameter β is determined by trial and error and the parameter δ is chosen to preserve the contrast between soft tissue and bone.

The first phantom, shown in Fig. 3 is a 256×256 density phantom consisting of four high-density "bone" disks ($\rho = 2$ gm/cm^3) immersed in a water disk ($\rho = 1$ gm/cm^3), which is surrounded by air ($\rho = 0$ gm/cm^3). The pixel size is 1.6 mm. The data were simulated over 500 angular steps and 600 radial bins, 1.3 mm each. The colorbar adjacent to Fig. 3 illustrates the gray scale window used to view all the images in the figure. The iterative algorithms ran for 20 iterations and 20 subsets.

Fig. 3(b) and (c) shows the reconstructed images (scaled to display density values) when algorithms that do not correct for beam hardening are used. Both FBP and PWLS-OS exhibit typical beam hardening artifacts: reduction in overall pixel values and dark streaks between high-density regions. Fig. 3(c) shows the importance of developing iterative algorithms based on polyenergetic physics.

Fig. 4(a) and (b) illustrates the image corrected by soft-tissue preprocessing and by the JS technique. The soft-tissue method, available on commercial scanners, leaves substantial artifacts. The JS technique postcorrects for most of the artifacts, but some persist. Simple thresholding (with threshold 1.5 gm/cm^3) of the soft-tissue-corrected FBP image provides the segmentation required by the JS technique.

The iterative reconstruction based on the polyenergetic model is shown in Fig. 4(c). The algorithm, was initialized with the JS-corrected image. The object was classified into bone or soft tissue by segmenting the JS-corrected FBP reconstruction using a density threshold of 1.5 gm/cm^3. We choose the segmentation threshold such that the number of mismatched pixels with the true object classification is minimum. In a more realistic setting, the true object is not available, and we hope to address the segmentation issue in future work. The iterative algorithm

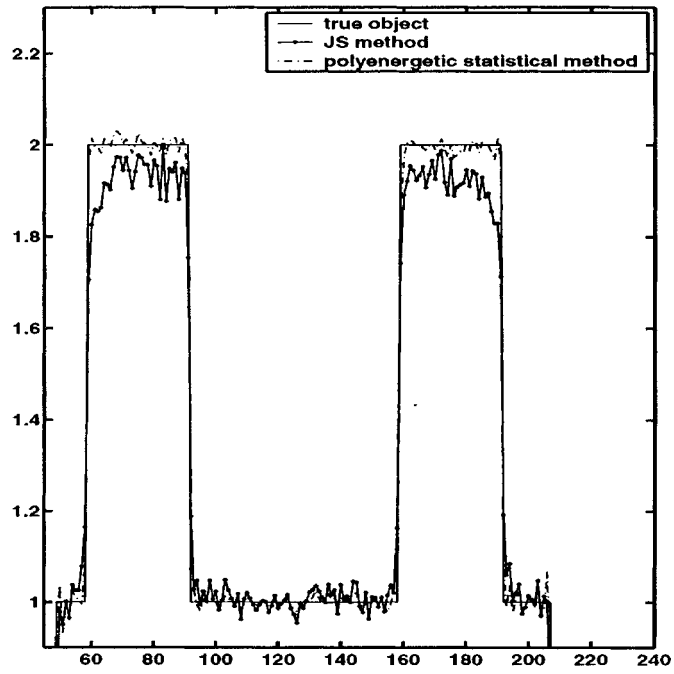

Fig. 5. Profile plots of reconstructed images.

TABLE I

Reconstruction Method	RMS Error
FBP	11.9 %
Soft Tissue	16.6 %
Joseph and Spital	4.9 %
Monoenergetic Iterative	9.6 %
Polyenergetic Iterative	2.2 %

significantly reduces artifacts, relative to JS, since it inherently accounts for the effects of broad energy spectrum. The profile plots in of the JS and the polyenergetic statistical algorithm images in Fig. 5 further delineate the difference in performance

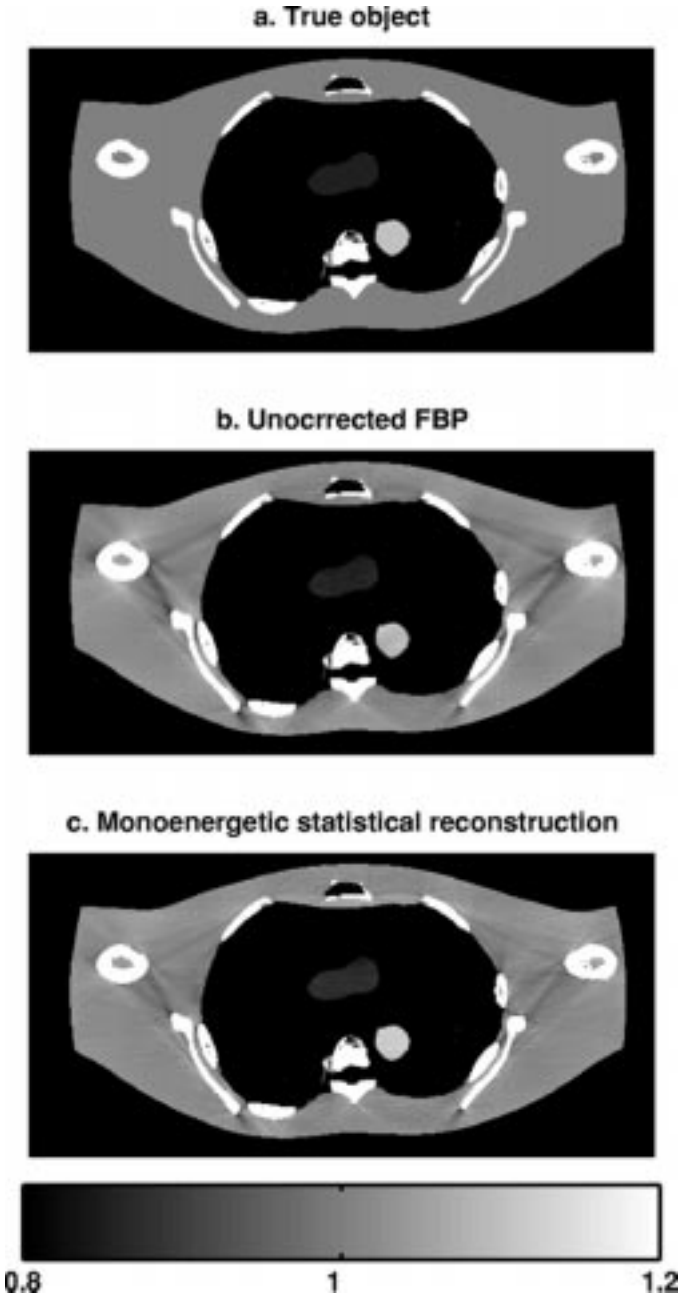

Fig. 6. True object and uncorrected FBP and statistical reconstruction.

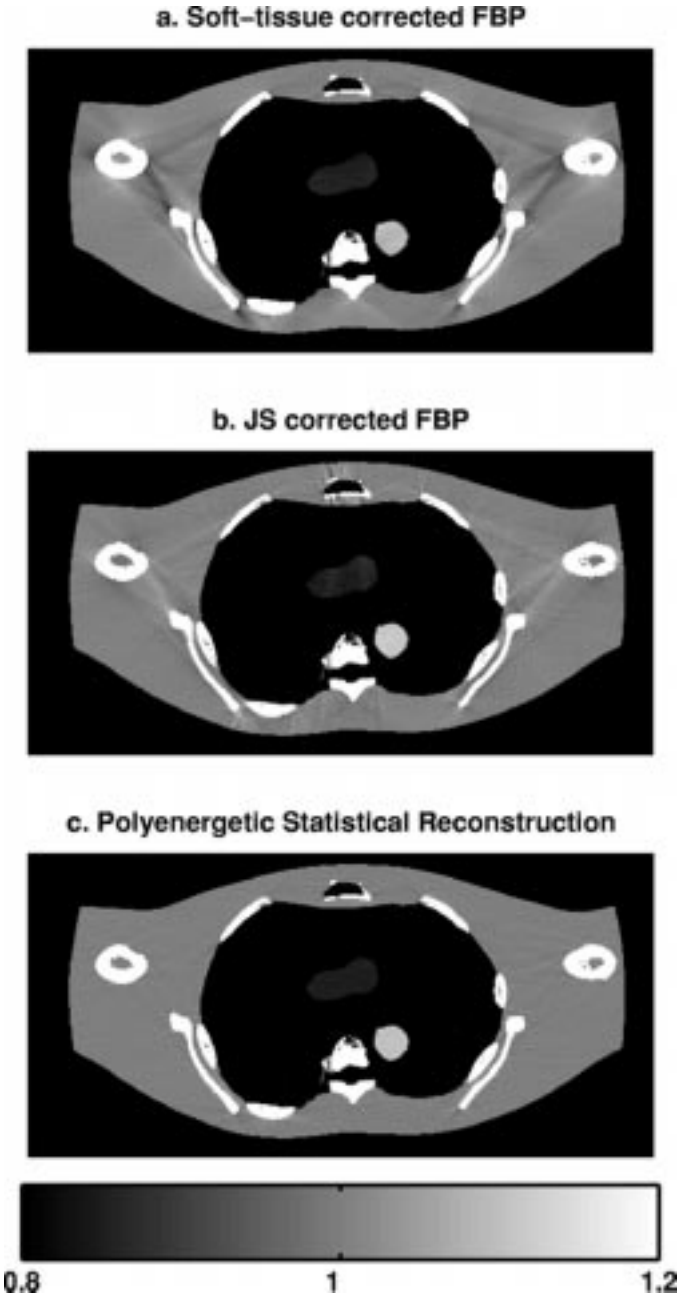

Fig. 7. Soft-tissue and JS-corrected FBP and polyenergetic statistical reconstruction.

between the two methods. Table I lists the root mean squared (RMS) error of all the methods, relative to the true object, and shows that the polyenergetic statistical reconstruction has the lowest error among all methods used. To compute the RMS error (and to display the images) for FBP and monoenergetic statistical reconstruction, their images were scaled by the appropriate mass attenuation coefficients to give density values.

To gain more confidence in our approach, we performed an additional experiment with this phantom where we simulated and reconstructed noise-free data (not shown). The results showed that polyenergetic iterative reconstruction was significantly more effective in reducing artifacts than JS, even when there was no noise. This is due to the fact that the iterative algorithm models the beam spectrum completely, whereas the JS method is approximate, even for noise-free data.

We also applied the different algorithms to the 512×250 object shown in Fig. 6(a). We created this "true" object by manually segmenting a previously acquired real CT image, then assigning density to each anatomical structure. The density of the bones is in the range 1.6–2 gm/cm^3 and the soft tissue densities vary from 0.9 to 1.1 gm/cm^3. The pixel size is 0.8 mm and the sinogram has 700 angular bins and 500 radial bins, 1.0 mm each. The statistical algorithms ran for 10 iterations and 50 subsets. We use the JS image to initialize the polyenergetic iterative technique and the soft-tissue-corrected image to determine the distribution of bone and soft-tissue regions with a threshold of 1.6 cm/gm^3. This threshold was chosen to minimize pixel mismatch with the true object.

The results are shown in Figs. 6 and 7. Uncorrected FBP and monoenergetic iterative algorithm images (scaled to display density values) suffer from beam-hardening artifacts, with streaks visible in the vicinity of bones. The soft-tissue, JS, and polyenergetic iterative results are also shown, with the latter clearly yielding less artifacts. Table II also lists the RMS error for all methods, with polyenergetic statistical reconstruction having smallest error.

For comparison, we also performed the polyenergetic reconstruction (not shown) with bone and water classification obtained from segmenting the true object. This yielded very similar results, so using the soft-tissue-corrected image to determine the f_j^ks appears to be a practical approach.

Like the JS method, the algorithm we propose requires knowledge of the spectrum and a presegmented image, but gives considerably improved density images. With the knowledge of the mass attenuation coefficient, one can scale the resulting density images to obtain attenuation coefficient information at any energy using (23).

V. Discussion

We have introduced a statistical iterative reconstruction algorithm for energy dependent X-ray attenuation that produces images with significantly reduced beam hardening artifacts. The algorithm is applicable for an arbitrary number of nonoverlapping materials, and we demonstrate its effectiveness for bone and soft tissue objects. Unlike most other transmission CT iterative algorithms, our algorithm is based on a realistic polyenergetic model. Figs. 3(c) and 6(c) illustrate the severe artifacts that result when an iterative algorithm based on a monoenergetic model reconstructs an image from polyenergetic data.

The algorithm we present requires knowledge of the incident spectrum and knowledge of the distribution of the different types of materials in the object. The spectrum can be measured [40] or determined through realistic simulations. Our results suggest that one can estimate the distribution of materials by segmenting a good FBP image, corrected with the soft-tissue technique. One could possibly improve on this approach by regenerating the segmentation after running one or more iterations of the proposed algorithm.

By successive applications of the optimization transfer principle, the statistical algorithm minimizes a separable paraboloidal surrogate, hence, it is parallelizable and fairly simple to implement. We also use ordered subsets and precomputed surrogate curvatures to accelerate convergence and reduce computation. When one subset is used with appropriate curvatures, the algorithm monotonically decreases the cost function. This is about the most that can be said about convergence since the cost function is inherently not convex.

When compared with the postprocessing technique of [18], the statistical algorithm yielded fewer artifacts. The JS method estimates the line-integral dependent nonlinearity for each sinogram bin and then recalculates the line integrals. The statistical method needs no such postprocessing since it inherently accounts for the nonlinearities. This is likely the reason for its superior performance.

Future work will include applying the polyenergetic approach to objects with three or more tissue types. The bone/soft-tissue model is sufficient for most cases, but a three-class model is necessary when contrast agents such as Iodine are introduced [21] and possibly when metallic implants are present. A further generalization of the algorithm is to allow for pixels that contain mixtures of two or more materials. This will enhance the accuracy of the algorithm, especially at material boundaries. This implies augmenting the set of variables with volume fractions to be estimated at every pixel. A promising approach for accomplishing this is to treat the material classes as random variables with a Markov random field model and to use joint likelihoods and penalties to jointly estimate pixel density values and material distribution [41], [42].

TABLE II

Reconstruction Method	RMS Error
FBP	8.2 %
Soft Tissue	17.1 %
Joseph and Spital	6.1 %
Monoenergetic Iterative	6.8 %
Polyenergetic Iterative	2.5 %

In reality, the X-ray CT detectors integrate over energy, and the actual distribution of the measurements is not Poisson. In order to improve the accuracy of reconstruction, a more realistic statistical model is necessary. One possibility is a model that considers the total signal a sum of scaled (by energy) Poisson processes each with a different scale factor [38]. This model is potentially more accurate because it accounts for the polyenergetic nature of the incident beam in the *detection* process.

Future work will also address some of the challenges posed by the PL approach. This approach has two important advantages. It improves the conditioning of the problem and enables one to choose penalty functions that control desired properties such as edge preservation. One drawback, however, is the absence of an intuitive method for choosing the values of the regularization parameters, which is often done by trial and error. This is inefficient and time consuming, and there is a need for a more systematic method for choosing the parameters. Another undesirable property of PL image reconstruction is its nonuniform spatial resolution [43]. A remedy for quadratic penalties exists [44]. For transmission imaging, we prefer to use the edge-preserving Huber penalty, for which the nonuniform resolution problem needs to be addressed.

Acknowledgment

The authors are grateful to P. Sukovic and S. Wilderman for supplying the spectrum of Fig. 2.

References

[1] I. Elbakri and J. A. Fessler, "Ordered subsets transmission reconstruction with beam hardening correction for x-ray CT," in *Proc. SPIE 4322, Medical Imaging 2001: Image Proc.*, vol. 1, 2001, pp. 1–12.

[2] J. A. Fessler, E. P. Ficaro, N. H. Clinthorne, and K. Lange, "Grouped-coordinate ascent algorithms for penalized likelihood transmission image reconstruction," *IEEE Trans. Med. Imag.*, vol. 16, pp. 166–175, Apr. 1997.

[3] C. Kamphius and F. J. Beekman, "Accelerated iterative transmission CT reconstruction using an ordered subsets convex algorithm," *IEEE Trans. Med. Imag.*, vol. 17, pp. 1101–1105, Dec. 1998.

[4] H. Erdoğan and J. A. Fessler, "Monotonic algorithms for transmission tomography," *IEEE Trans. Med. Imag.*, vol. 18, pp. 801–814, Sept. 1999.
[5] ——, "Ordered subsets algorithms for transmission tomography," *Phys. Med. Biol.*, vol. 44, pp. 2835–2851, 1999.
[6] H. M. Hudson and R. S. Larkin, "Accelerated image reconstruction using ordered subsets of projection data," *IEEE Trans. Med. Imag.*, vol. 13, pp. 601–609, Dec. 1994.
[7] K. Lange and R. Carson, "EM reconstruction algorithms for emission and transmission tomography," *J. Comput. Assist. Tomogr.*, vol. 8, no. 2, pp. 306–316, Apr. 1984.
[8] S. H. Manglos, G. M. Gange, A. Krol, F. D. Thomas, and R. Narayanaswamy, "Transmission maximum-likelihood reconstruction with ordered subsets for cone beam CT," *Phys. Med. Biol.*, vol. 40, pp. 1225–1241, 1995.
[9] B. De Man, J. Nuyts, P. Dupont, G. Marchal, and P. Suetens, "Reduction of metal artifacts in X-ray computed tomography using a transmission maximum *a posteriori* algorithm," *IEEE Trans. Nucl. Sci.*, vol. 47, pp. 977–981, June 2000.
[10] G. Wang, M. W. Vannier, and P. C. Cheng, "Iterative X-ray cone beam tomography for metal artifact reduction and local region reconstruction," *Microscopy Microanal.*, vol. 5, pp. 58–65, 1999.
[11] A. H. Delaney and Y. Bresler, "Globally convergent edge-preserving regularized reconstruction: An application to limited-angle tomography," *IEEE Trans. Image Processing*, vol. 7, pp. 104–221, Feb. 1998.
[12] J. Nuyts, B. De Man, E. Dupont, M. Defrise, E. Suetens, and L. Mortelmans, "Iterative reconstruction for helical CT: A simulation study," *Phys. Med. Biol.*, vol. 43, pp. 729–737, 1998.
[13] A. P. Dempster, N. M. Laird, and D. B. Rubin, "Maximum likelihood from incomplete data via the EM algorithm," *J. Roy. Statist. Soc. Ser. B*, vol. 39, no. 1, pp. 1–38, 1977.
[14] K. Lange, M. Bahn, and R. Little, "A theoretical study of some maximum likelihood algorithms for emission and transmission tomography," *IEEE Trans. Med. Imag.*, vol. MI-6, pp. 106–114, June 1987.
[15] J. A. Browne and T. J. Holmes, "Developments with maximum likelihood X-ray computed tomography," *IEEE Trans. Med. Imag.*, vol. 11, pp. 40–52, Mar. 1992.
[16] C. A. Bouman and K. Sauer, "A unified approach to statistical tomography using coordinate descent optimization," *IEEE Trans. Image Processing*, vol. 5, pp. 480–492, Mar. 1996.
[17] K. Sauer and C. A. Bouman, "A local update strategy for iterative reconstruction from projections," *IEEE Trans. Signal Processing*, vol. 41, pp. 553–548, Feb. 1993.
[18] P. M. Joseph and R. D. Spital, "A method for correcting bone induced artifacts in computed tomography scanners," *J. Comput. Assist. Tomogr.*, vol. 2, pp. 100–108, 1978.
[19] J. M. Meagher, C. D. Mote, and H. B. Skinner, "CT image correction for beam hardening using simulated projection data," *IEEE Trans. Nucl. Sci.*, vol. 37, pp. 1520–1524, Aug. 1990.
[20] O. Nalcioglu and R. Y. Lou, "Post-reconstruction method for beam hardening in computerized tomography," *Phys. Med. Biol.*, vol. 24, no. 2, pp. 330–340, 1979.
[21] P. M. Joseph and C. Ruth, "A method for simultaneous correction of spectrum hardening artifacts in CT images containing both bone and iodine," *Med. Phys.*, vol. 24, no. 10, pp. 1629–1634, Oct. 1997.
[22] J. Hsieh, R. C. Molthen, C. A. Dawson, and R. H. Johnson, "An iterative approach to the beam hardening correction in cone beam CT," *Med. Phys.*, vol. 27, no. 1, pp. 23–29, Jan. 2000.
[23] A. C. Kak and M. Slaney, *Principles of Computerized Tomographic Imaging*. Piscataway, NJ: IEEE Press, 1988.
[24] R. E. Alvarez and A. Macovski, "Energy-selective reconstruction in X-ray computerized tomography," *Phys. Med. Biol.*, vol. 21, no. 5, pp. 733–744, 1976.
[25] S. S. Gleason, H. Sari-Sarraf, M. J. Paulus, D. K. Johnson, S. J. Norton, and M. A. Abidi, "Reconstruction of multienergy X-ray computer tomography images of laboratory mice," *IEEE Trans. Nucl. Sci.*, vol. 46, pp. 1081–1086, Aug. 1999.
[26] P. Sukovic and N. H. Clinthorne, "Penalized weighted least-squares image reconstruction in single and dual energy X-ray computed tomography," *IEEE Trans. Med. Imag.*, vol. 19, pp. 1075–1091, Nov. 2000.
[27] C. H. Yan, R. T. Whalen, G. S. Beaupré, S. Y. Yen, and S. Napel, "Reconstruction algorithm for polychromatic CT imaging: Application to beam hardening correction," *IEEE Trans. Med. Imag.*, vol. 19, pp. 1–11, Jan. 2000.
[28] B. De Man, J. Nuyts, P. Dupont, G. Marchal, and P. Suetens, "An iterative maximum-likelihood polychromatic algorithm for CT," *IEEE Trans. Med. Imag.*, vol. 20, pp. 999–1008, Oct. 2001.
[29] D. L. Snyder, C. W. Helstrom, A. D. Lanterman, M. Faisal, and R. L. White, "Compensation for read-out noise in charge-coupled-device images," *J. Opt. Soc. Amer.*, vol. 12, no. 2, pp. 273–283, Feb. 1995.
[30] J. A. Fessler, "Hybrid Poisson/polynomial objective functions for tomographic image reconstruction from transmission scans," *IEEE Trans. Image Processing*, vol. 4, pp. 1439–1449, Oct. 1995.
[31] A. R. De Pierro, "On the relation between the ISRA and the EM algorithm for positron emission tomography," *IEEE Trans. Med. Imag.*, vol. 12, pp. 38–333, June 1993.
[32] ——, "A modified expectation maximization algorithm for penalized likelihood estimation in emission tomography," *IEEE Trans. Med. Imag.*, vol. 14, pp. 132–137, Mar. 1995.
[33] R. A. Brooks and G. D. Chiro, "Beam hardening in X-ray reconstruction tomography," *Phys. Med. Biol.*, vol. 21, no. 3, pp. 390–398, 1976.
[34] J. H. Hubbell and S. M. Seltzer. Tables of X-ray mass attenuation coefficients and mass energy-absorption coefficients. [Online]. Available: http://physics.nist.gov/PhysRefData/XrayMassCoef/.
[35] J. Beutel, H. L. Kundel, and R. L. Van Metter, Eds., *Handbook of Medical Imaging*. Bellingham, WA: SPIE, 2000, vol. 1.
[36] D. F. Yu, J. A. Fessler, and E. P. Ficaro, "Maximum likelihood transmission image reconstruction for overlapping transmission beams," *IEEE Trans. Med. Imag.*, vol. 19, pp. 1094–1105, Nov. 2000.
[37] J. A. Fessler, "Statistical image reconstruction methods for transmission tomography," in *Handbook of Medical Imaging, Medical Image Processing and Analysis*, M. Sonka and J. M. Fitzpatrick, Eds. Bellingham, WA: SPIE, 2000, vol. 2, pp. 1–70.
[38] B. R. Whiting, L. J. Montagnino, and D. G. Politte, "Modeling X-ray computed tomography sinograms," *Med. Phys.*, 2001, submitted for publication.
[39] P. Sukovic and N. H. Clinthorne, "Design of an experimental system for dual energy X-ray CT," in *Proc. IEEE Nuclear Science Symp. Medical Imaging Conf.*, vol. 2, 1999, pp. 1021–1022.
[40] C. H. Yan, R. T. Whalen, G. S. Beaupre, S. Y. Yen, and S. Napel, "Modeling of polychromatic attenuation using computed tomography reconstructed images," *Med. Phys.*, vol. 26, no. 4, pp. 631–642, Apr. 1999.
[41] Y. Zhang, J. A. Fessler, N. H. Clinthorne, and W. L. Rogers, "Experimental evaluation for joint estimation approach," in *Proc. IEEE Nuclear Science Symp. Medical Imaging Conf.*, vol. 3, 1996, pp. 1623–1627.
[42] J. E. Bowsher, V. E. Johnson, T. G. Turkington, R. J. Jaszczak, C. E. Floyd, and R. E. Coleman, "Bayesian reconstruction and use of anatomical *a priori* information for emission tomography," *IEEE Trans. Med. Imag.*, vol. 15, pp. 673–686, Oct. 1996.
[43] J. A. Fessler and W. L. Rogers, "Spatial resolution properties of penalized-likelihood image reconstruction methods: Space-invariant tomography," *IEEE Trans. Image Processing*, vol. 5, pp. 1346–1358, Sept. 1996.
[44] J. W. Stayman and J. A. Fessler, "Regularization for uniform spatial resolution properties in penalized likelihood image reconstruction," *IEEE Trans. Med. Imag.*, vol. 19, pp. 601–615, June 2000.